

CDeFuse: Continuous Decomposition for Infrared and Visible Image Fusion

Haolong Ma¹, Hui Li¹, Chunyang Cheng¹, Xiaoning Song¹, and Zhongwei Shen²

¹ Jiangnan University

{lihui.cv, x.song}@jiangnan.edu.cn
ninesxd@qq.com, chunyang_cheng@163.com

² Jiangsu University of Science and Technology
shenzw@usts.edu.cn

Abstract. As a common image processing technique, image decomposition is often used to extract complementary information between modalities. In current decomposition-based image fusion methods, typically, source images are decomposed into three parts at single scale (*i.e.*, visible-exclusive part, infrared-exclusive part, and common part) and lacking interaction between modalities during the decomposition process. These results in the inability of fusion images to effectively focus on finer complementary information between modalities at various scales. To address the above issue, a novel decomposition mechanism, Continuous Decomposition Fusion (CDeFuse), is proposed. Firstly, CDeFuse extends the original three-part decomposition to a more general K -part decomposition at each scale through similarity constraints to fuse multi-scale information and achieve a finer representation of decomposition features. Secondly, a Continuous Decomposition Module (CDM) is introduced to assist K -part decomposition. Its core component, State Transformer (ST), efficiently captures complementary information between modalities by utilizing multi-head self-attention mechanism. Finally, a novel decomposition loss function and the corresponding computational optimization strategy are utilized to ensure the smooth progress of the decomposition process while maintaining linear growth in time complexity with the number of decomposition results K . Extensive experiments demonstrate that our CDeFuse achieves comparable performance compared to previous methods. The code will be publicly available.

Keywords: Image Fusion · Image Decomposition · Multimodality

1 Introduction

As a fundamental field of image processing, image fusion seeks to create informative and visually appealing images by extracting the most significant information from various source images [33, 37, 39, 42]. One of the notable challenges in image processing is Infrared and Visible Image Fusion (IVIF), which entails integrating complementary and advantageous information from distinct modalities [9, 25, 44].

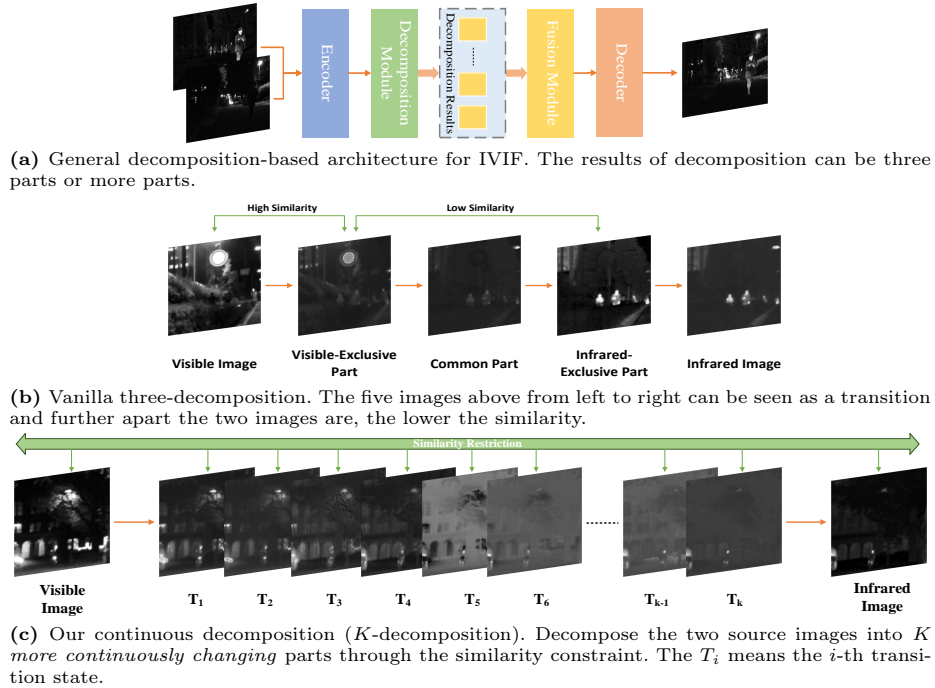


Fig. 1: Workflow of general decomposition-based models and comparison of Vanilla three-decomposition with our proposed continuous decomposition.

In the IVIF task, the input comprises both infrared and visible images. Visible images are distinguished by their abundant texture information, which aligns more closely with human visual perception. However, they are susceptible to lighting variations, occlusion, and other factors, resulting in the loss of vital information. In contrast, infrared images excel in highlighting targets in extreme conditions (*e.g.*, low light) by capturing thermal radiation but are prone to noise. Consequently, in IVIF tasks, the fused image must mitigate the shortcomings of both modalities to achieve superior visual quality [7].

Numerous methods have emerged recently to address the issues in IVIF task [10, 13, 17, 24, 31, 36]. A prevalent and effective approach among these methods involves decomposing source images into three parts: two exclusive and one common. As illustrated in Fig. 1a, the process commences with the encoder extracting useful features from the source images. Subsequently, these features are sent to a feature decomposition module for decomposition into the aforementioned three parts. These parts are then fed into the fusion module for integration and decoding, generating the final fused image. For example, in DeFusion [15], two encoders, denoted as E and E^c , are employed to extract comprehensive representation features and common features, respectively. These features are inputted into three decoders for decomposition and decoding, yielding two unique

parts, f_u^1 and f_u^2 , and a common part, f_c . Finally, these parts are concatenated channel-wise to obtain the fused feature, from which the final fused image is derived through a linear transformation.

However, despite the success of DeFusion in decomposing the source images, it overlooks the interaction among the decomposed features. CDDFuse [46] drives the decomposition process using the Correlation Coefficient (CC), with the aim of maximizing the correlation between the common parts and minimizing that of the unique parts. Inspired by CDDFuse, we extend the decomposition process to approximate continuity by imposing similarity constraints, thereby further refining the decomposition results. Specifically, we interpret the three results of image decomposition as a transition from one source image to another.

As depicted in Fig. 1b, we traverse from one source image to its unique part, then to the common part shared by both images, followed by the unique part of another image, and ultimately to the latter image. We term these three decomposed parts as transition states. Illustrated in Fig. 1c, assuming K transition states between one source image and another, their relationship is constrained by similarity. Compared to the original three-part decomposition, this continuous process, although not strictly continuous, offers a more refined representation of information and can better retain the details of the source image. Thus, we denote this process as continuous decomposition. Moreover, to maximize the utilization of complementary information across modalities, we introduce State Attention during decomposition to facilitate interaction between the two modalities.

The contributions of our work are summarized as follows:

(i) A novel continuous decomposition concept is proposed to represent source image features more meticulously.

(ii) A novel decomposition module (termed as CDM) is proposed to capture more complementary information between transition states while facilitating continuous decomposition.

(iii) We devise a new loss function to steer the decomposition process. Moreover, to mitigate computational expenses, a simple yet efficient strategy, termed as Support Decomposition Strategy (SDS), is introduced to reduce the time complexity and preserve effective decomposition.

2 Related Work

2.1 Deep Learning-Based Methods

Deep learning, renowned for its robust feature representation and adaptability, has become ubiquitous in IVIF task [6, 18, 45, 47]. Unlike traditional methods reliant on manual feature engineering, deep learning offer the flexibility to extract features tailored for fused images, yielding superior results in both visual and downstream tasks [34, 43]. Presently, Convolutional Neural Network (CNN) and Transformer stand as the two prevailing network architectures employed in IVIF task.

CNN, characterized by its strong generalization ability and robustness, is commonly utilized in image fusion. For instance, Li *et al.* [11] utilize CNN as both encoder and decoder to extract effective features and reconstruct images, respectively. To effectively fuse objects of varying scales, many networks integrate multi-scale structures to better capture objects across different scales [4, 8, 23]. For example, SGFusion [16] adopts U-Net as a backbone to fuse features guided by saliency information at different scales, thereby enhancing the model’s robustness.

Transformer is initially introduced by Vaswani *et al.* [28] and achieves remarkable success in Natural Language Processing (NLP). Subsequently, Dosovitskiy *et al.* [3] successfully transpose Transformer into Computer Vision (CV). In Transformer, the multi-head self-attention (MHSA) mechanism serves as the core component. Endowed with potent long-distance dependency modeling capabilities and minimal inductive bias, MHSA aptly captures the complementary relationships between modalities in IVIF [12, 21, 27].

2.2 Image Decomposition Methods

Before the rise of deep learning, the field of image fusion predominantly relies on traditional models based on decomposition [1, 14, 20]. For instance, Wang *et al.* [29] introduce a decomposition model grounded in the Laplacian pyramid and employ a handcrafted fusion strategy to merge components at each level. However, these traditional models, with their manually designed decomposition and fusion strategies, lack adaptability and flexibility.

With the advent of deep learning, researchers begin exploring neural networks for image decomposition [2, 35]. Liang *et al.* [15] pioneer a method employing self-supervised learning for image decomposition, fusion, and reconstruction. This approach leverages a vast number of unpaired images for training, thus mitigating the issue of insufficient data pairs in image fusion. However, its failure to consider complementary information while decomposition renders it inadequate for tasks demanding strong complementarity.

CDDFuse [46], on the other hand, utilizes similarity to guide image decomposition, decomposing the image into common and unique parts for fusion. Nevertheless, its network structure overlooks multi-scale information and considers only the decomposition of the source image into three parts, leading to decomposition results that fail to effectively represent features in a refined manner.

In this study, we prioritize a more nuanced multi-scale decomposition and employ the multi-head self-attention mechanism to enhance the capture of complementary information.

3 Proposed Method

In this section, we first introduce the workflow of our model and the detailed design of each module. Then, we provide the formulas for calculating the loss function we proposed and explain the underlying design principles.

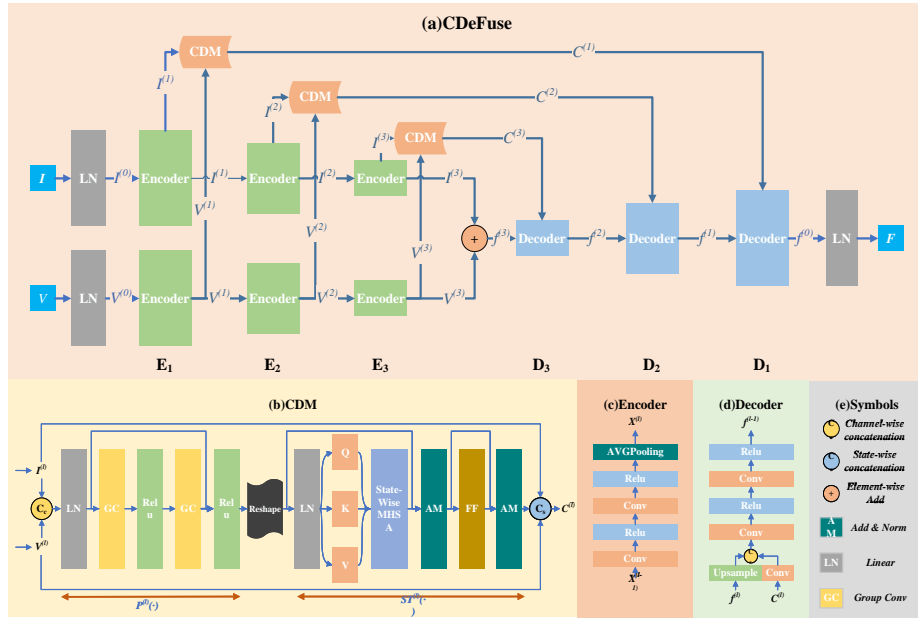


Fig. 2: The architecture of CDeFuse, when the number of levels is 3. (a) The pipeline of CDeFuse, where E_l and D_l denote the l -th level of Encoder and Decoder respectively. (b, c, d) The internal structure diagrams for CDM, Encoder and Decoder in the l -th level respectively, where the X of Encoder can be V or I . (e) Abbreviations and names of symbols used in this figure.

3.1 Overview

CDeFuse is mainly composed of three types of modules, *i.e.*, Encoder, Decoder and CDM. Encoder and Decoder are respectively responsible for extracting shallow features from the source images and reconstructing the fused image. CDM is used for interaction between modalities. In addition to the above three types of modules, there are two linear transformations at the input and output positions of our model to process the transformation of the number of channels.

As shown in Fig. 2(a), we adopt a U-net-like multi-scale structure. The Encoder and Decoder have three levels and are marked $E_l, D_l (l \in \{1, 2, 3\})$ respectively. For a more general discussion, we set the number of levels of our model to N and the number of decomposition results to K in this section.

3.2 Encoder

As shown in Fig. 2(c), the Encoder is composed of 3×3 convolutions with padding, ReLU activation functions, and 2×2 average pooling and shared for both infrared and visible images at the same level. The Encoder is responsible for extracting shallow features from both infrared and visible images for subsequent feature decomposition.

For ease of model description, we introduce the following notation: $EN^{(l)}(\cdot)$, $DE^{(l)}(\cdot, \cdot)$, $CDM^{(l)}(\cdot, \cdot)$ respectively denote the Encoder, Decoder, and CDM of the l -th level. Let $I, V \in R^{H \times W}$ denote the input infrared and visible images. Based on the notation defined above, the processing of input by the l -th level encoder can be expressed as follows:

$$\begin{aligned} I^{(l)} &= EN^{(l)}(I^{(l-1)}), V^{(l)} = EN^{(l)}(V^{(l-1)}) \\ l &\in \{1, 2, \dots, N\} \end{aligned} \quad (1)$$

where $I^{(0)}$ and $V^{(0)}$ are obtained by linear transformation of the sources image I and V respectively.

3.3 Continuous Decomposition Module

The Continuous Decomposition Module(CDM) is employed to decompose the infrared and visible images into several transition states. To achieve this, it is necessary to first extract information within each transition states from the input images, and then obtain complementary information between modalities.

As illustrated in Fig. 2 (b), to accomplish the former, linear transformations and group convolutions are employed. Linear transformations are responsible for generating preliminary transition states. Group convolutions further decompose and extract finer information within each transition state.

Concretely, we employ 3×3 convolutions with padding and set the number of groups to K . Then, we obtained K transition states denoted as $S \in R^{K \times C \times \hat{H} \times \hat{W}}$, where C represents the number of channels, and $\hat{H} \times \hat{W}$ represents the size of the feature maps of transition states. We denote the sub-module in CDM using a linear transformation, group convolutions and ReLU activation function as $P(\cdot)$.

State Transformer To maximize the utilization of complementary information between modalities, we introduce the State Transformer, denoted as $ST(\cdot)$. It captures inter-modality complementary information by applying multi-head self-attention along the transition state wise.

To achieve this, we first generate Q, K , and V from S , which is accomplished through linear transformations. Then, we reshape and split Q, K , and V into multiple attention heads, yielding $\hat{Q}, \hat{K}, \hat{V} \in R^{K \times E}$, where $E \times h = C \times \hat{H} \times \hat{W}$ and h denotes the number of attention heads. Next, standard multi-head self-attention is applied along the transition state wise. State Attention can be formalized as follows:

$$\begin{aligned} Q &= \Phi_Q(S), K = \Phi_K(S), V = \Phi_V(S) \\ Atten &= softmax(\hat{Q} \cdot \hat{K}^T / \sqrt{E}) \\ T &= \phi_p(\hat{V} \cdot Atten) + S \end{aligned} \quad (2)$$

where $\Phi(\cdot)$, $\phi(\cdot)$ represent 3×3 and 1×1 convolutions respectively and T denotes the result of State Attention. For the FeedForward network(FF) component of

State Transformer, we adopt the GDFN proposed in Restormer [41], which focuses on obtaining fine complementary information through the gate mechanism.

In summary, for the l -th CDM module $CDM^{(l)}(\cdot, \cdot)$, we can express its transformation in the following form:

$$\begin{aligned} S^{(l)} &= P^{(l)}([V^{(l)}; I^{(l)}|c]), T^{(l)} = ST^{(l)}(S^{(l)}) \\ C^{(l)} &= [V^{(l)}; T^{(l)}; I^{(l)}|s] \\ l &\in \{1, 2, \dots, N\} \end{aligned} \quad (3)$$

where $[\cdot; |c]$, $[\cdot; |s]$ denote concatenation operators along the channel wise and state wise respectively. The symbols mentioned above are added indexes with l to indicate they belong to the l -th CDM. For instance, $ST^{(l)}$ represents the State Transformer in the l -th CDM.

3.4 Decoder

The Decoder is used for feature fusion and image reconstruction. Specifically, different levels of the Decoder perform feature fusion and image reconstruction at their respective scales. The Decoder conducts elementary feature fusion of the CDM's results through a 3×3 convolution. Subsequently, as illustrated in Fig. 2(d), this result is concatenated with the upsampled output of the previous level Decoder along the channel wise. Then, through two 3×3 convolutions with padding and ReLU activation functions, further fusion and reconstruction of the image result at this scale are performed.

In summary, the l -th Decoder can be expressed as follows:

$$\begin{aligned} f^{(N)} &= I^{(N)} + V^{(N)} \\ f^{(l-1)} &= DE^{(l)}(f^{(l)}, C^{(l)}) \\ l &\in \{1, 2, \dots, N\} \end{aligned} \quad (4)$$

where we perform element-wise addition on the outputs of the N -th level Encoder to obtain $f^{(N)}$, which serves as the input to the N -th level Decoder. The fused image F can be generated through a linear transformation from $f^{(0)}$.

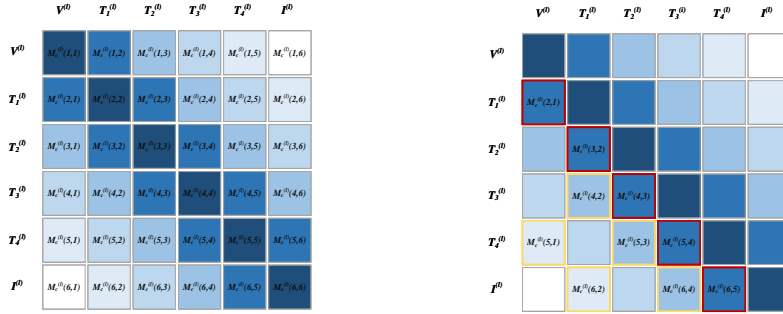
3.5 Loss Function

The loss function L_{all} consists of three parts and can be written as follows:

$$L_{all} = L_{int} + \alpha_1 L_{decom} + \alpha_2 L_{grad} \quad (5)$$

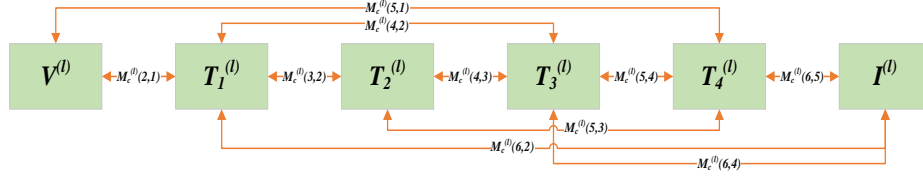
where L_{decom} is the decomposition loss, $L_{int} = \frac{1}{HW} \|F - \max(I, V)\|_F^2$ is the pixel-level loss, $L_{grad} = \frac{1}{HW} \| |\nabla F| - \max(|\nabla I|, |\nabla V|) \|_F^2$ is the gradient loss, α_1, α_2 are parameters used to trade-off them, and ∇ denotes the Sobel operator.

To achieve continuous decomposition, we need to impose similarity constraints among transition states as well as the source image feature maps. First,



(a) An example of $M_c^{(l)}$ in the l -th level when $K = 4$. The depth of color represents the constraint of similarity, with darker colors indicating higher similarity.

(b) An example of SDS in the l -th level when $K = 4$. The yellow boxes represent randomly sampled constraints, while the red boxes represent those calculated consistently each time.



(c) A more illustrative example of Fig. 3b, where arrows between features represent similarity constraints.

Fig. 3: Schematic diagrams illustrating the key principles of decomposition loss calculation.

we calculate the similarity $\mu = CC(V, I)$ between the two source images V and I using the CC metric. As shown in Fig. 3a, for the output $C^{(l)}$ of the l -th level CDM, we compute pairwise similarities along the state-wise, resulting in a symmetric similarity matrix M_c . The similarity matrix $M_c^{(l)}$ of the l -th level is:

$$M_c^{(l)}(i, j) = CC(C_{i,\cdot}^{(l)}, C_{j,\cdot}^{(l)}) \quad (6)$$

$$i, j \in \{1, 2, \dots, K + 2\}$$

where i, j are matrix indices, $C_{i,\cdot}^{(l)}, C_{j,\cdot}^{(l)}$ denote the i -th and j -th features in the l -th level. According to formula Eq. (3), the feature can be a transition state or a feature of the source images at l -th level. Since the matrix is symmetric, we only analyze its lower triangular part.

By constraining the similarity matrix M_c , we are able to drive the decomposition. Analyzing the matrix M_c , the values on the main diagonal of the matrix are 1. For the lower left corner $M_c^{(l)}(K + 2, 1)$, we approximate it to the similarity between the source images μ . For the remaining positions of the similarity, we gradually decay them from 1 to μ along the direction from the main diagonal to the lower left corner. Thus, we construct a target matrix M_t :

$$M_t^{(l)}(i, j) = \Omega(i - j, \mu, K + 2) \quad (7)$$

$$i, j \in \{1, 2, \dots, K + 2\}$$

where $\Omega(\cdot, \cdot, \cdot)$ is a decay function used to calculate the similarity during the decay process. We design two decay functions, linear decay and Gaussian decay, with formulas as follows:

$$\begin{aligned}\Omega_l(p, \mu, s) &= 1 - p \frac{1 - \mu}{s - 1} \\ \Omega_g(p, \mu, s) &= \exp\left(-\frac{p^2}{2 * \sigma}\right) \\ \text{where } \sigma &= -\frac{(s - 1)^2}{2 \ln(\mu)}\end{aligned}\tag{8}$$

where Ω_l and Ω_g represent linear decay and Gaussian decay, respectively. Linear decay reduces the similarity with a fixed step size, while Gaussian decay follows the form of a Gaussian function. We adopt linear decay, as detailed in the experiment in Sec. 5.2.

In summary, the decomposition loss L_{decom} can be written as:

$$\begin{aligned}L_{decom} &= \frac{2}{N(K^2 + 3K)} \sum_{l=1}^N \|M_c^{(l)} - M_t^{(l)}\|_F^2 \\ \text{s.t. } M_c^{(l)}(1, K + 2) &= M_t^{(l)}(1, K + 2) = 0 \\ M_c^{(l)}(K + 2, 1) &= M_t^{(l)}(K + 2, 1) = 0\end{aligned}\tag{9}$$

It is worth noting that we do not constrain $M_c^{(l)}(1, K + 2)$ and $M_c^{(l)}(K + 2, 1)$ because they are unrelated to the transition states and represents the similarity between features of the two source images. Moreover, since the values on the main diagonal are always 1, we do not impose constraints on them. Therefore, the number of similarities constrained is $\frac{1}{2}((K + 2)^2 - (K + 2) - 2) = \frac{1}{2}(K^2 + 3K)$. In practice, we only calculate the lower triangular part.

3.6 Support Decomposition Strategy

The time complexity of the decomposition loss L_{decom} is approximately $O(K^2)$. This means that as the number of transition states K increases, the computational cost of the decomposition loss will grow quadratically.

In order to enhance the scalability of the model, we propose the Support Decomposition Strategy (SDS). Instead of constraining the similarities of all feature pairs, we only constrain a subset of them. Concretely, we constrain only the similarities of adjacent features, along with a portion of randomly sampled similarities.

For example, as shown in Figs. 3b and 3c, when the number of transition states is 4, we restrain the similarities of adjacent features (red portion) and additionally constrain a portion of randomly sampled similarities (yellow portion). Statistically, when the number of training epochs and the amount of training data are sufficient, this method can approximate the desired decomposition,

thus reducing the time complexity. For a more general case with K transition states, in the l -th level, we define the sampling strategy as follows:

$$SDS(\beta) = \{(i+1, i)\}_{i=1}^{K+1} \cup \{(u_i, v_i)\}_{i=1}^{K+1} \quad (10)$$

s.t. $u_i \neq K+2, v_i \neq 1, u_i+1 \neq v_i, u_i > v_i, u_i, v_i \in \{1, 2, \dots, K+2\}$

where $SDS(\beta)$ represents the sampled constraints' indexes with random seed β , $\{(u_i, v_i)\}_{i=1}^{K+1}$ is a set of randomly sampled ordered pairs and $|SDS(\beta)| = 2K+2$.

Based on the sampling results described above, we can rewrite the decomposition loss as follows:

$$L_{decom} = \frac{1}{N(2K+2)} \sum_{l=1}^N \sum_{(i,j) \in SDS(*)} (M_c^{(l)}(i, j) - M_t^{(l)}(i, j))^2 \quad (11)$$

where $*$ denotes the random number seed determined by the operating system. Clearly, through SDS, we control the time complexity of the decomposition loss to the $O(K)$ level, greatly improving the scalability of our model.

4 Experiments

4.1 Setup

Implementation Details The numbers of levels and transition states in our model is set to $N = 4$ and $K = 9$. Training images are randomly cropped to a size of 192×192 , while using random flipping as a data augmentation technique. The batch size is set to 30, and we train for 1600 epochs. AdamW [19] as the optimizer and WarmupCosine as the learning rate adjustment strategy are used. We opt for a linear decay function as the decay strategy Eq. (8) for calculating the decomposition loss. The hyperparameters α_1 and α_2 are both set to 3. All experiments are conducted on a NVIDIA GeForce RTX 3090 Ti.

Datasets and Metrics Our model is trained on the training set of MSRS [26]. For the test set, we test on RoadScene [33] dataset, the test set of MSRS [26] and 14 pairs of images from TNO. We employ five metrics, (standard deviation)SD [22], (mutual information)MI, Qabf [38], (visual information fidelity)VIF [5], and (structural similarity index measure)SSIM [32], to evaluate the our model's performance. Higher scores indicate better performance for all metrics.

4.2 Comparison with Other Methods

Seven existing methods are chosen to conduct the comparison experiments, include two autoencoder-based methods (DenseFuse [11] and SwinFuse [30]), two decomposition-based models (CDDFuse [46] and DeFusion [46]), two unified models (U2Fusion [33] and DeFusion [15]), an end-to-end method (DAT-Fuse [27]), and one diffusion-based model (Dif-fusion [40]).



Fig. 4: Qualitative comparison of the image "FLIR_00069" in the RoadScene dataset.

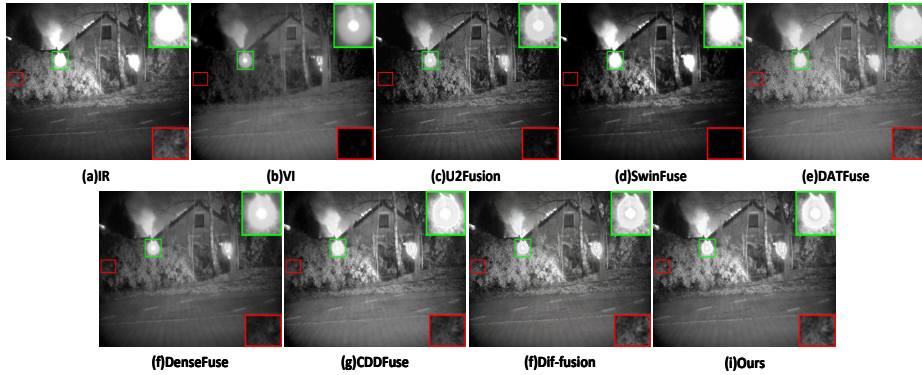


Fig. 5: Qualitative comparison of the image "14" in the TNO dataset.

Qualitative Comparison Figs. 4 and 5 illustrate the qualitative comparison. Clearly, our method preserves more texture information while better highlighting salient regions. For example, in the areas marked by red and green boxes in Fig. 4, our method exhibits higher contrast and is more consistent with human visual perception. In the regions marked by red and green boxes in Fig. 5, our method retains more detailed texture information. This enables our method to better restore real scenes even in extreme low-light condition.

Quantitative Comparison Tabs. 1 to 3 present the quantitative comparison of our method. Our model achieves competitive performance in most metrics, demonstrating the effectiveness of our approach. It is worth noting that we only trained on MSRS [26] without fine-tuning on other datasets. This indicates the strong generalization ability of our method.

4.3 Visualization of Transition States

Fig. 6 displays the visualization results related to the transition states. Transition state feature maps $\{T_1^{(1)}, T_2^{(1)}, \dots, T_9^{(1)}\}$ at the first level, along with the features of visible and infrared images $\{V^{(1)}, I^{(1)}\}$, are selected for visual analysis. From

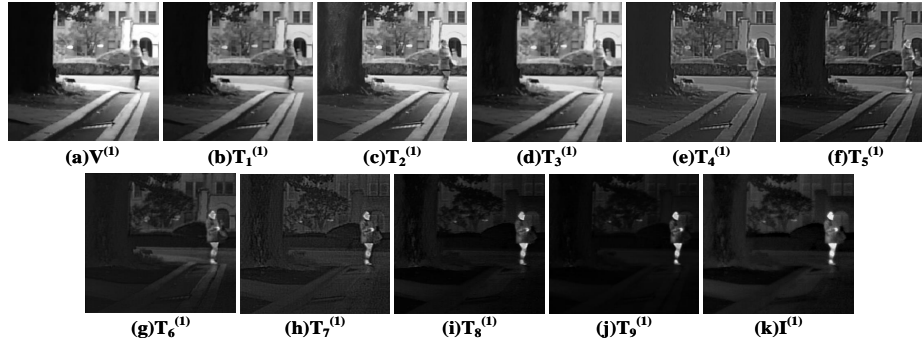


Fig. 6: Visualization of transition states and two source images' feature maps in 1-th level.

Table 1: Qualitative comparison on the MSRS [26] dataset. The bold and underlined parts represent the best and second-best values respectively.

	VIF	Qabf	MI	SSIM	SD
DeFusion	0.76	0.53	3.35	<u>0.46</u>	37.91
Dif-fuison	0.83	0.58	3.33	0.45	41.90
U2Fusion	0.52	0.29	2.28	0.32	26.05
DenseFuse	0.69	0.36	2.64	0.45	23.57
SwinFuse	0.36	0.18	1.78	0.17	29.72
DATFuse	0.91	0.64	3.89	0.45	36.48
CDDFuse	<u>1.05</u>	<u>0.69</u>	<u>5.00</u>	0.51	43.37
CDeFuse(Ours)	1.06	0.72	5.05	0.51	<u>42.47</u>

left to right and top to bottom, the feature maps exhibit a continuous changing trend, consistent with the viewpoints discussed above.

It is evident that these decomposed states are not mutually exclusive. There are overlapping regions and unique parts within each transition state, with each capturing some finer details. For instance, $T_7^{(1)}$ extracts and focuses on edge information from both source images, while $T_9^{(1)}$ emphasizes information in the foreground region. This facilitates better preservation of detail information, thereby enhancing the quality of the fused image.

Table 2: Qualitative comparison on the TNO dataset. The bold and underlined parts represent the best and second-best values respectively.

	VIF	Qabf	MI	SSIM	SD
DeFuse	0.55	0.36	2.62	0.42	33.43
Dif-fuio	0.57	0.46	2.82	0.42	40.91
U2Fuse	0.59	0.47	2.10	0.47	36.63
DenseFuse	0.64	0.45	2.42	0.47	34.14
SwinFuse	0.67	0.44	2.48	0.45	54.52
DATFuse	0.64	0.47	3.03	0.46	28.55
CDDFuse	<u>0.75</u>	<u>0.54</u>	<u>3.14</u>	0.50	<u>46.28</u>
CDeFuse(Ours)	0.80	0.60	3.62	<u>0.48</u>	41.28

Table 3: Qualitative comparison on the RoadScene dataset. The bold and underlined parts represent the best and second-best values respectively.

	VIF	Qabf	MI	SSIM	SD
DeFuse	0.47	0.34	2.91	0.42	34.57
Dif-fuio	0.55	0.51	2.91	0.44	42.56
U2Fuse	0.56	0.40	2.89	0.46	37.51
DenseFuse	0.56	0.39	2.91	0.48	32.21
SwinFuse	<u>0.64</u>	<u>0.50</u>	2.95	0.48	58.28
DATFuse	0.60	0.47	3.63	0.46	31.75
CDDFuse	0.62	0.48	3.00	0.48	<u>56.32</u>
CDeFuse(Ours)	0.65	0.57	<u>3.00</u>	<u>0.47</u>	42.33

Table 4: The ablation experiments on the number of transition states K . The bold indicates the best value.

Configs	VIF	MI	SSIM
$K = 3$	0.62	2.71	0.46
$K = 5$	0.64	2.89	0.45
$K = 7$	0.65	2.96	0.46
$K = 9$	0.65	3.00	0.47
$K = 11$	0.64	2.90	0.46

Table 5: Other ablation experiments. The bold indicates the best value. The GD means Gaussian decay.

Configs	VIF	MI	SSIM	FLOPs↓
I w/o SDS	0.65	3.09	0.46	10152M
II w/o CDM	0.62	2.80	0.45	N/A
III w/o ST	0.64	2.92	0.46	N/A
IV w/o L_{decom}	0.63	2.90	0.45	N/A
V using GD	0.64	3.05	0.46	N/A
VI Ours	0.65	3.00	0.47	3760M

5 Ablation Studies

The ablation experiments were conducted to confirm the rationality of module design, the effectiveness of decomposition loss, and the appropriateness of parameter selection. All experiments are trained on the MSRS [26] training set and

tested on the RoadScene dataset. We selected three metrics, namely VIF, MI, and SSIM, to measure the effectiveness of the fusion results.

5.1 The Number of States

To find the suitable number of transition states K , we conducted an ablation experiment. Following the tradition of the three-decomposition method, we started with $K = 3$ and increased by two transition states for each experiment. As shown in Tab. 4, it can be observed that as K increases, the performance of the model gradually improves. When K approaches 9, the performance improvement slows down and shows a tendency to decline. Therefore, considering the overall performance of the model, setting $K = 9$ is reasonable.

5.2 Other Factors

In this subsection, we conducted ablation experiments on other factors of our model. The uppercase Roman numerals in Tab. 5 are used to denote specific experiments. For example, Exp.*I* denotes the first row experiment in the table.

Loss Function We removed the decomposition loss L_{decom} while retaining the CDM module to demonstrate the effectiveness of the decomposition loss in Exp.*IV*. Additionally, we test the impact of using the Gaussian decay function from Eq. (8) on the decomposition process in Exp.*V*. The results showed that using Linear as the decay strategy had better results. We speculate that this might be because the linear decay provides a more balanced change, which is more suitable for representing unique detailed information in each transition state.

Continuous Decomposition Module To verify the effectiveness of the CDM module, in Exp.*II*, we discarded the CDM module while maintaining a parameter size similar to the original network. Similarly, to validate the effectiveness of the State Transformer, in Exp.*III*, we replaced the State Transformer with a convolutional neural network of comparable parameter size. The results showed that the CDM module has a positive effect on the quality of image fusion, and the ST module can better capture complementary information between modalities.

Support Decomposition Strategy SDS aims to reduce the computation required for model training. To compare the impact of the SDS on model’s performance, we conducted experiments without SDS under the condition of $K = 9$. As shown in Exp.*I* and Exp.*VI*, the results of our method without SDS are very similar to those with SDS. This demonstrates the effectiveness of SDS. We also compared the FLOPs required to compute the L_{decom} for both the use and non-use of SDS, to verify the actual impact of SDS on reducing computational cost.

6 Conclusion

In this paper, a novel continuous decomposition based fusion method is proposed for infrared and visible image fusion task. With the help of the proposed continuous decomposition module and efficient decomposition loss function, the source images can be decomposed into multiple transition states making the fused image can focus on more details. Meanwhile, during the decomposition process, the model can better capture complementary information between modalities through the use of our State Transformer. Experimental results demonstrate that our proposed method achieves comparable or even better performance.

References

1. Burt, P.J., Kolczynski, R.J.: Enhanced image capture through fusion. In: 1993 (4th) international Conference on Computer Vision. pp. 173–182. IEEE (1993) [4](#)
2. Di, J., Ren, L., Liu, J., Guo, W., Zhange, H., Liu, Q., Lian, J.: Fdnet: An end-to-end fusion decomposition network for infrared and visible images. *Plos one* **18**(9), e0290231 (2023) [4](#)
3. Dosovitskiy, A., Beyer, L., Kolesnikov, A., Weissenborn, D., Zhai, X., Unterthiner, T., Dehghani, M., Minderer, M., Heigold, G., Gelly, S., et al.: An image is worth 16x16 words: Transformers for image recognition at scale. *International Conference on Learning Representations* (2021) [4](#)
4. Gan, W., Wu, X., Wu, W., Yang, X., Ren, C., He, X., Liu, K.: Infrared and visible image fusion with the use of multi-scale edge-preserving decomposition and guided image filter. *Infrared Physics & Technology* **72**, 37–51 (2015) [4](#)
5. Han, Y., Cai, Y., Cao, Y., Xu, X.: A new image fusion performance metric based on visual information fidelity. *Information fusion* **14**(2), 127–135 (2013) [10](#)
6. He, C., Li, K., Xu, G., Zhang, Y., Hu, R., Guo, Z., Li, X.: Degradation-resistant unfolding network for heterogeneous image fusion. In: *Proceedings of the IEEE/CVF international conference on computer vision*. pp. 12611–12621 (2023) [3](#)
7. Hermessi, H., Mourali, O., Zagrouba, E.: Multimodal medical image fusion review: Theoretical background and recent advances. *Signal Processing* **183**, 108036 (2021) [2](#)
8. Li, B., Lu, J., Liu, Z., Shao, Z., Li, C., Du, Y., Huang, J.: Aefusion: A multi-scale fusion network combining axial attention and entropy feature aggregation for infrared and visible images. *Applied Soft Computing* **132**, 109857 (2023) [4](#)
9. Li, C., Zhang, B., Hong, D., Yao, J., Chanussot, J.: Lrr-net: An interpretable deep unfolding network for hyperspectral anomaly detection. *IEEE Transactions on Geoscience and Remote Sensing* (2023) [1](#)
10. Li, H., Qi, X., Xie, W.: Fast infrared and visible image fusion with structural decomposition. *Knowledge-Based Systems* **204**, 106182 (2020) [2](#)
11. Li, H., Wu, X.J.: Densfuse: A fusion approach to infrared and visible images. *IEEE Transactions on Image Processing* **28**(5), 2614–2623 (2018) [4](#), [10](#)
12. Li, H., Wu, X.J.: Crossfuse: A novel cross attention mechanism based infrared and visible image fusion approach. *Information Fusion* **103**, 102147 (2024) [4](#)
13. Li, J., Huo, H., Li, C., Wang, R., Feng, Q.: Attentionfgan: Infrared and visible image fusion using attention-based generative adversarial networks. *IEEE Transactions on Multimedia* **23**, 1383–1396 (2020) [2](#)

14. Li, S., Kang, X., Hu, J.: Image fusion with guided filtering. *IEEE Transactions on Image processing* **22**(7), 2864–2875 (2013) [4](#)
15. Liang, P., Jiang, J., Liu, X., Ma, J.: Fusion from decomposition: A self-supervised decomposition approach for image fusion. In: *European Conference on Computer Vision*. pp. 719–735. Springer (2022) [2](#), [4](#), [10](#)
16. Liu, J., Dian, R., Li, S., Liu, H.: Sgfusion: A saliency guided deep-learning framework for pixel-level image fusion. *Information Fusion* **91**, 205–214 (2023) [4](#)
17. Liu, J., Fan, X., Huang, Z., Wu, G., Liu, R., Zhong, W., Luo, Z.: Target-aware dual adversarial learning and a multi-scenario multi-modality benchmark to fuse infrared and visible for object detection. In: *Proceedings of the IEEE/CVF Conference on Computer Vision and Pattern Recognition*. pp. 5802–5811 (2022) [2](#)
18. Liu, J., Fan, X., Jiang, J., Liu, R., Luo, Z.: Learning a deep multi-scale feature ensemble and an edge-attention guidance for image fusion. *IEEE Transactions on Circuits and Systems for Video Technology* **32**(1), 105–119 (2021) [3](#)
19. Loshchilov, I., Hutter, F.: Decoupled weight decay regularization. *International Conference on Learning Representations* (2019) [10](#)
20. Nikolov, S., Hill, P., Bull, D., Canagarajah, N.: Wavelets for image fusion. *Wavelets in Signal and Image Analysis: From Theory to Practice* pp. 213–241 (2001) [4](#)
21. Rao, D., Xu, T., Wu, X.J.: Tgfuse: An infrared and visible image fusion approach based on transformer and generative adversarial network. *IEEE Transactions on Image Processing* (2023) [4](#)
22. Rao, Y.J.: In-fibre bragg grating sensors. *Measurement science and technology* **8**(4), 355 (1997) [10](#)
23. Sun, L., Li, Y., Zheng, M., Zhong, Z., Zhang, Y.: Mcnet: Multiscale visible image and infrared image fusion network. *Signal Processing* **208**, 108996 (2023) [4](#)
24. Tang, L., Deng, Y., Ma, Y., Huang, J., Ma, J.: Superfusion: A versatile image registration and fusion network with semantic awareness. *IEEE/CAA Journal of Automatica Sinica* **9**(12), 2121–2137 (2022) [2](#)
25. Tang, L., Xiang, X., Zhang, H., Gong, M., Ma, J.: Divfusion: Darkness-free infrared and visible image fusion. *Information Fusion* **91**, 477–493 (2023) [1](#)
26. Tang, L., Yuan, J., Zhang, H., Jiang, X., Ma, J.: Piafusion: A progressive infrared and visible image fusion network based on illumination aware. *Information Fusion* **83**, 79–92 (2022) [10](#), [11](#), [12](#), [13](#)
27. Tang, W., He, F., Liu, Y., Duan, Y., Si, T.: Datfuse: Infrared and visible image fusion via dual attention transformer. *IEEE Transactions on Circuits and Systems for Video Technology* (2023) [4](#), [10](#)
28. Vaswani, A., Shazeer, N., Parmar, N., Uszkoreit, J., Jones, L., Gomez, A.N., Kaiser, Ł., Polosukhin, I.: Attention is all you need. *Advances in neural information processing systems* **30** (2017) [4](#)
29. Wang, W., Chang, F.: A multi-focus image fusion method based on laplacian pyramid. *J. Comput.* **6**(12), 2559–2566 (2011) [4](#)
30. Wang, Z., Chen, Y., Shao, W., Li, H., Zhang, L.: Swinfuse: A residual swin transformer fusion network for infrared and visible images. *IEEE Transactions on Instrumentation and Measurement* **71**, 1–12 (2022) [10](#)
31. Wang, Z., Wang, J., Wu, Y., Xu, J., Zhang, X.: Unfusion: A unified multi-scale densely connected network for infrared and visible image fusion. *IEEE Transactions on Circuits and Systems for Video Technology* **32**(6), 3360–3374 (2021) [2](#)
32. Wang, Z., Bovik, A.C.: A universal image quality index. *IEEE signal processing letters* **9**(3), 81–84 (2002) [10](#)

33. Xu, H., Ma, J., Jiang, J., Guo, X., Ling, H.: U2fusion: A unified unsupervised image fusion network. *IEEE Transactions on Pattern Analysis and Machine Intelligence* **44**(1), 502–518 (2020) [1](#), [10](#)
34. Xu, H., Ma, J., Le, Z., Jiang, J., Guo, X.: Fusiondn: A unified densely connected network for image fusion. In: *Proceedings of the AAAI conference on artificial intelligence*. vol. 34, pp. 12484–12491 (2020) [3](#)
35. Xu, H., Wang, X., Ma, J.: Drf: Disentangled representation for visible and infrared image fusion. *IEEE Transactions on Instrumentation and Measurement* **70**, 1–13 (2021) [4](#)
36. Xu, H., Zhang, H., Ma, J.: Classification saliency-based rule for visible and infrared image fusion. *IEEE Transactions on Computational Imaging* **7**, 824–836 (2021) [2](#)
37. Xu, R., Xiao, Z., Yao, M., Zhang, Y., Xiong, Z.: Stereo video super-resolution via exploiting view-temporal correlations. In: *Proceedings of the 29th ACM International Conference on Multimedia*. pp. 460–468 (2021) [1](#)
38. Xydeas, C.S., Petrovic, V., et al.: Objective image fusion performance measure. *Electronics letters* **36**(4), 308–309 (2000) [10](#)
39. Yang, Z., Yao, M., Huang, J., Zhou, M., Zhao, F.: Sir-former: Stereo image restoration using transformer. In: *Proceedings of the 30th ACM International Conference on Multimedia*. pp. 6377–6385 (2022) [1](#)
40. Yue, J., Fang, L., Xia, S., Deng, Y., Ma, J.: Dif-fusion: Towards high color fidelity in infrared and visible image fusion with diffusion models. *IEEE Transactions on Image Processing* (2023) [10](#)
41. Zamir, S.W., Arora, A., Khan, S., Hayat, M., Khan, F.S., Yang, M.H.: Restormer: Efficient transformer for high-resolution image restoration. In: *Proceedings of the IEEE/CVF conference on computer vision and pattern recognition*. pp. 5728–5739 (2022) [7](#)
42. Zhang, H., Xu, H., Tian, X., Jiang, J., Ma, J.: Image fusion meets deep learning: A survey and perspective. *Information Fusion* **76**, 323–336 (2021) [1](#)
43. Zhang, H., Xu, H., Xiao, Y., Guo, X., Ma, J.: Rethinking the image fusion: A fast unified image fusion network based on proportional maintenance of gradient and intensity. In: *Proceedings of the AAAI conference on artificial intelligence*. vol. 34, pp. 12797–12804 (2020) [3](#)
44. Zhang, X., Demiris, Y.: Visible and infrared image fusion using deep learning. *IEEE Transactions on Pattern Analysis and Machine Intelligence* (2023) [1](#)
45. Zhao, F., Zhao, W., Yao, L., Liu, Y.: Self-supervised feature adaption for infrared and visible image fusion. *Information Fusion* **76**, 189–203 (2021) [3](#)
46. Zhao, Z., Bai, H., Zhang, J., Zhang, Y., Xu, S., Lin, Z., Timofte, R., Van Gool, L.: Cddfuse: Correlation-driven dual-branch feature decomposition for multi-modality image fusion. In: *Proceedings of the IEEE/CVF Conference on Computer Vision and Pattern Recognition*. pp. 5906–5916 (2023) [3](#), [4](#), [10](#)
47. Zhou, H., Wu, W., Zhang, Y., Ma, J., Ling, H.: Semantic-supervised infrared and visible image fusion via a dual-discriminator generative adversarial network. *IEEE Transactions on Multimedia* (2021) [3](#)